BNL-212371-2019-JAAM

Silver-Containing α-MnO2 Nanorods: Electrochemistry in Rechargeable Aqueous Zn-MnO2 Batteries

L. Wang,

To be published in "Journal of The Electrochemical Society"

October 2019

Interdisciplinary Science Department

Brookhaven National Laboratory

U.S. Department of Energy

USDOE Office of Science (SC), Basic Energy Sciences (BES) (SC-22)

Notice: This manuscript has been authored by employees of Brookhaven Science Associates, LLC under Contract No. DE-SC0012704 with the U.S. Department of Energy. The publisher by accepting the manuscript for publication acknowledges that the United States Government retains a non-exclusive, paid-up, irrevocable, world-wide license to publish or reproduce the published form of this manuscript, or allow others to do so, for United States Government purposes.

DISCLAIMER

This report was prepared as an account of work sponsored by an agency of the United States Government. Neither the United States Government nor any agency thereof, nor any of their employees, nor any of their contractors, subcontractors, or their employees, makes any warranty, express or implied, or assumes any legal liability or responsibility for the accuracy, completeness, or any third party's use or the results of such use of any information, apparatus, product, or process disclosed, or represents that its use would not infringe privately owned rights. Reference herein to any specific commercial product, process, or service by trade name, trademark, manufacturer, or otherwise, does not necessarily constitute or imply its endorsement, recommendation, or favoring by the United States Government or any agency thereof or its contractors or subcontractors. The views and opinions of authors expressed herein do not necessarily state or reflect those of the United States Government or any agency thereof.

Silver-Containing α-MnO_2 Nanorods: Electrochemistry in Rechargeable Aqueous Zn-MnO_2 Batteries

Lei Wang,[1] Qiyuan Wu,[1] Alyson Abraham,[2] Patrick J. West,[3] Lisa M. Housel,[2] Gurpreet Singh,[2] Nahian Sadique,[2] Calvin D. Quilty,[2] Daren Wu,[3] Esther S. Takeuchi,[1,2,3,*,z] Amy C. Marschilok,[1,2,3,,z] and Kenneth J. Takeuchi[2,3,z]**

[1]*Energy Sciences Directorate, Brookhaven National Laboratory, Upton, New York 11973, USA*
[2]*Department of Chemistry, Stony Brook University, Stony Brook, New York 11794, USA*
[3]*Department of Materials Science and Chemical Engineering, Stony Brook University, Stony Brook, New York 11794, USA*

The reduction and subsequent oxidation of silver hollandite nanorods, $Ag_{1.5}Mn_8O_{16}$, were explored in aqueous $ZnSO_4$ electrolyte for the first time. The impact of reduction on the electrodes was probed where images of recovered cathodes were collected to evaluate the changes in morphology, structural, and electrochemical properties as a function of varying potential. Ag metal particle formation upon reduction was observed on reduction through a reduction-displacement reaction as confirmed by SEM/EDS, XRD, and XAS results accompanied by a decrease in charge transfer impedance, as determined by electrochemical impedance spectroscopy. On charge, in contrast to the reduction/oxidation electrochemistry in non-aqueous media where irreversible formation of silver metal was observed, disappearance of the silver metal is observed indicating oxidation of the silver centers is facilitated in aqueous electrolyte.
© The Author(s) 2019. Published by ECS. This is an open access article distributed under the terms of the Creative Commons Attribution 4.0 License (CC BY, http://creativecommons.org/licenses/by/4.0/), which permits unrestricted reuse of the work in any medium, provided the original work is properly cited. [DOI: 10.1149/2.0101915jes]

Manuscript submitted July 22, 2019; revised manuscript received September 6, 2019. Published October 23, 2019.

Rechargeable aqueous Zn/MnO_2 batteries are considered viable alternatives to lithium ion batteries for some applications owing to the high abundance and safety associated with both Zn and MnO_2, along with the intrinsic nonflammability and the high ionic conductivity of the aqueous electrolyte.[1–4] In traditional alkaline electrolyte systems, several irreversible byproducts usually form on the anode (ZnO or $Zn(OH)_2$) and the cathode ($Mn(OH)_2$, Mn_3O_4, and Mn_2O_3), resulting in capacity fade and poor Coulombic efficiencies.[5,6] Recently, neutral or mild acidic aqueous electrolytes were utilized in rechargeable aqueous Zn/MnO_2 battery to improve the electrochemical function.[7,8] Charge/discharge mechanisms for MnO_2 have been reported to be either reversible Zn^{2+} [2,9,10] and/or H^{+}[1] insertion/extraction.[7] Hollandite-type α-MnO_2 materials are of interest from an electrochemical perspective due to their high surface area to volume nanorod morphology, ability to accommodate a wide array of ions into their structural tunnels (K^+,Ag^+,Li^+,Na^+,Zn^{2+}) and synthetic versatility.[6,11] Structurally, α-MnO_2 materials are composed of MnO_6 octahedral double chains that are edge- and corner-sharing with adjacent double chains in the plane to form (2 × 2) tunnel structures, that can accommodate different tunnel cations.[12] α-MnO_2 nanofibers were previously used as a cathode material in mild aqueous $ZnSO_4$-based electrolyte, which demonstrated an operating voltage of 1.44 V, and a capacity of 285 mAh/g at C/3 rate attributed to a chemical conversion reactions between α-MnO_2 and H^+.[1] Nanofibers of α-MnO_2 prepared hydrothermally were previously reported to reduce via a Zn^{2+} insertion mechanism with the reversible formation of the layered manganese oxide birnessite.[13] A microemulsion synthesis of α-MnO_2 material delivered capacity of 210 mAh/g at 0.5C,[2] while in a separate study, α-MnO_2 nanorods delivered an initial capacity of 233 mAh/g and gradually faded to 147 mAh/g in cycle 15 at a current density of 83 mA/g.[14]

Recently, Ag^+ stabilized hollandites ($Ag_xMn_8O_{16}$) have been extensively explored as cathode materials in Li-ion[12,15] and Na-ion[6,12] based nonaqueous battery systems. Silver ions are located in the α-MnO_2 tunnels to stabilize the tunnels and it has been observed that the presence of Ag^+ reduces the a, b dimensions of the unit cell relative to a material with no metal cation located in the tunnel.[12,16] Ag^+ hollandite exhibited formation of conductive Ag^0 nanoparticles upon discharge through a reduction-displacement reaction.[6,12] The presence of Ag^0 nanoparticles has been linked to lower cell resistances and improved electronic conductivity.[17] Interestingly, previous studies in nonaqueous battery systems[6,18] have indicated a significant difference in the lithiation versus sodiation process of the $Ag_xMn_8O_{16}$ materials. Specifically, a significant decrease in charge transfer resistance after 1.5 electron equivalents per $Ag_{1.2}Mn_8O_{16}$formula unit of Na ion insertion was observed while in contrast, gradual impedance increase was noted during lithiation.[6] The impedance decrease upon sodiation was coincident with the formation of silver metal during the early discharge process, while Ag formation can be only detected after 6 electron equivalents of lithiation in the lithium system,[18] which indicated the earlier formation of silver metal during the sodiation process relative to the lithation process. Given the strong electrochemical foundation of $Ag_xMn_8O_{16}$ (x = 1.2-1.6) in organic electrolyte batteries, it is worthwhile to probe if the positive attributes of Ag^+ stabilized hollandite are translatable to other electrochemical cell chemistries, specifically the aqueous Zn system.

Two recent reports have recently evaluated the role of zinc intercalation when a metal cation (either Ag^+ or Cu^{2+}) is included in a vanadium oxide-based cathode.[19,20] For example, in aqueous Zn/$Ag_{0.4}V_2O_5$ cells, a combination of a displacement and intercalation mechanism (CDI) was reported for Zn^{2+} insertion. The CDI can be described as providing two options for Zn^{2+} insertion, where in the displacement process the transition metal cation (i.e. Ag^+) would be replaced by Zn^{2+} and in the intercalation process the Zn^{2+} would (de)insert into vacant sites in the V_2O_5 host structure. Displacement of Ag^+ by Zn^{2+} was demonstrated by the appearance of a $Zn_2(V_3O_8)_2$ phase upon discharging (to 0.4V vs. Zn/Zn^{2+}), and a disappearance of this phase upon charging to 1.4 V. This reversible peak growth was attributed to Zn^{2+}/Ag^+ displacement reaction during Zn^{2+} insertion/extraction which also resulted in the formation of the reduction of silver from Ag^+ to Ag^0, forming conductive Ag^0 network.[19] In aqueous Zn/copper pyrovanadate ($Cu_3(OH)_2V_2O_7{\cdot}2H_2O$) cells, a reduction-displacement mechanism was reported to stem from the insertion of Zn^{2+} to the reduction of Cu^{2+} to mixed Cu^0/Cu^+ and partial vanadium reduction from V^{5+} to V^{4+}. Upon charging to 1.4V, most of the Cu^0/Cu^+ was oxidized back to Cu^+/Cu^{2+} and the vanadium was oxidized back to V^{5+}. During discharge, the insertion of Zn^{2+} lead to a new phase of zinc vanadate ($Zn_{0.25}V_2O_5{\cdot}H_2O$), which was characterized by ex situ XRD and HRTEM. Simultaneous to Zn^{2+} insertion was the reduction of Cu^{2+} to mixed Cu^+/Cu^0, verified by ex situ XPS, and HRTEM/EDS noting preference for Cu^0 nanoparticle formation on the surface. While

*Electrochemical Society Fellow.
**Electrochemical Society Member.
zE-mail: esther.takeuchi@stonybrook.edu; amy.marschilok@stonybrook.edu; kenneth.takeuchi.1@stonybrook.edu

Downloaded on 2019-11-06 to IP 130.199.221.173 address. Redistribution subject to ECS terms of use (see ecsdl.org/site/terms_use) unless CC License in place (see abstract).

general reversibility was observed upon charging, there was some Zn^{2+} that did not extract fully and was attributed to be the underlying reason for observed capacity fade.[20] Additionally, mixed vanadium valence cathodes and the incorporation of potassium into Mn_8O_{16} were also shown to improve charge transport or reduce Mn dissolution in ZIB. A mixed vanadium valence cathode (V^{4+}-V_2O_5) was prepared from VOOH, which was subsequently used in aqueous Zn cells with 2M $ZnSO_4$ electrolyte. The presence of V^{4+} was attributed to the increased electrochemical activity, reduced polarization and enhanced charge transport when compared to V_2O_5,[21] and the incorporation of potassium into Mn_8O_{16} with oxygen defect sites was also shown to suppress manganese dissolution.[22]

There have been no prior reports utilizing $Ag_xMn_8O_{16}$ compositions as cathode materials for rechargeable aqueous Zn/MnO_2 batteries. Herein, $Ag_{1.5}Mn_8O_{16}$ nanorods were prepared using a facile reflux method, and subsequently tested as cathode materials for aqueous Zn/MnO_2 batteries in $ZnSO_4$ based electrolyte. The impact of tunnel Ag^+ ions on the resulting electrochemistry was probed through the use of cyclic voltammetry, galvanostatic discharge, scanning electrochemical microscopy, X-ray diffraction, X-ray photoelectron spectroscopy, scanning electron microscopy and X-ray micro- fluorescence spectroscopy. A reaction mechanism specific to the $Ag_{1.5}Mn_8O_{16}$ materials in aqueous zinc ion batteries has been proposed supported by the results of the various characterization techniques.

Experimental

Synthesis and characterization of $Ag_{1.5}Mn_8O_{16}$ nanorods.— $Ag_{1.5}Mn_8O_{16}$ nanorods were synthesized through a reflux procedure in ambient atmosphere as previously reported.[12,23] Briefly, aqueous $MnSO_4$ was added dropwise to an $AgMnO_4$ solution and then brought to reflux conditions for 15 hours. The resulting material was isolated, washed with deionized H_2O and dried. The materials were heat treated at 300°C for 6 hours in air prior to use.

XRD analysis was performed on a Rigaku MiniFlex 600 using copper K-alpha radiation, indexed with the silver hollandite crystal structure[24] and matched via Rietveld Refinement. Crystallite size was determined using the Scherrer equation applied to the (211) peak at 37° 2θ. Chemical composition analysis of cationic species was performed using a Thermo-Fisher iCAP-6300 Inductively Coupled Plasma – Optical Emission Spectrometer (ICP-OES). Oxygen content was estimated through thermogravimetric analysis (TGA) using a TA Instruments Q600.

Electrochemical measurements.—Electrodes were prepared by combining $Ag_{1.5}Mn_8O_{16}$, carbon and poly vinylidene difluoride at a weight ratio of 7:2:1 in N-methyl pyrrolidone and casting the slurry onto stainless steel foil. The active mass loading is ~1.5 mg/cm^2. Coin type cells were assembled using $Ag_{1.5}Mn_8O_{16}$ electrodes, glass fiber separators and Zn foil with 2 M $ZnSO_4$ aqueous electrolyte.

Cyclic voltammetry (CV) testing was performed in a two-electrode coin cell with $Ag_{1.5}Mn_8O_{16}$ as cathode and zinc metal as counter and reference electrodes, using a Bio-Logic potentiostat at a scan rate of 0.2 mV/s. Charge-discharge behavior in a voltage window between 1.0-1.8V was conducted using a Maccor testing system. Electrochemical impedance spectra (EIS) were obtained over a frequency range of 1 MHz to 10mHz, with an AC amplitude of 10 mV using a Bio-Logic potentiostat. All the electrochemical measurements were performed at 30°C.

Scanning vibrating probe (SVP) is an alternating current (AC) technique which measures the potential difference between the two end-positions of the vibrating probe (across vibration amplitude) due to ionic current flow in the electrolyte solution.[25–28] The SVP experiment was conducted using a commercially available instrument (Bio-Logic, M470) in 0.5 M $ZnSO_4$(aq) with a three electrode set up as shown in

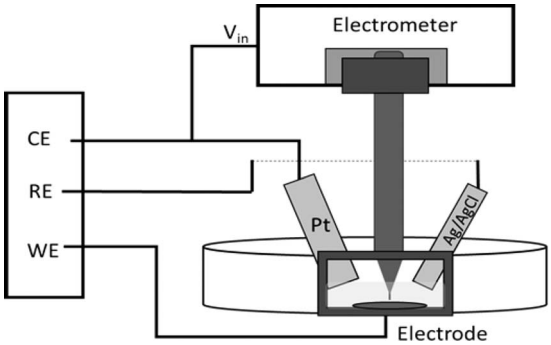

Figure 1. Schematic of Scanning Vibrating Probe (SVP) experimental setup, where the probe vibrates along the z direction and scans over the x-y plane.

Figure 1. The $Ag_{1.5}Mn_8O_{16}$ electrode (70/20/10, active/carbon/PVDF) on stainless steel foil current collector was affixed to a Bio-Logic cell and leveled using a spirit level to prevent sample tilt. The electrode sample on stainless steel foil was used as the working electrode, with an Ag/AgCl reference electrode (RE), and a Pt counter electrode (CE). The input voltage (V_{in}) of the electrometer was connected to the counter electrode to provide a stable potential in which the potential difference was measured in the electrolyte solution of 0.5M aqueous zinc sulfate ($ZnSO_4$). Constant potential measurements were carried out for 10 minutes at 0.8V and 0.6V (v. Zn/Zn^{2+}) followed by an SVP measurement after each reduction. SVP measurements were performed on a scan area up to 2mm by 4mm using a 25μm step size, at a scanning velocity of 1000 μm/s with a line delay of 2 seconds. The constant potential-SVP measurements were performed sequentially without changing the sample or the probe-sample distance. The probe-sample distance was ~100μm, with a vibration amplitude of 30μm.

Post-electrochemical testing analysis of $Ag_{1.5}Mn_8O_{16}$ electrodes.— Scanning electron microscopy and energy dispersive X-ray spectroscopy (SEM-EDX) analysis of the electrodes were conducted using a JEOL 7600F instrument equipped with an EDX detector. SEM-EDX analysis was performed over the pristine sample and samples (dis)charged at different potentials. All the electrodes were rinsed with deionized water to remove residual electrolyte salts prior to data collection. SEM images were collected using a low-angle backscattered electron detector.

X-ray microfluorescence (μ-XRF) mapping with corresponding ex-situ Mn K-edge X-ray absorption near edge structure (XANES) measurements were collected at 5-ID of the National Synchrotron Light Source II (NSLS-II) at Brookhaven National Laboratory. Self-supporting electrodes were fabricated with silver hollandite active material and carbon nanotubes (1:1 mass ratio) as described previously.[29,30] After electrochemical testing, the working electrodes were recovered, rinsed, and sealed between polyimide film. The energy of the beam was calibrated using a Mn reference foil at 6539 eV. During mapping, the energy was set to 6700 eV. The collected XANES spectra were background subtracted, aligned, and normalized using the Athena software package.[31]

XRD and XAS analyses were conducted on samples recovered after discharge to 1.0 V, and a sample discharged to 1.0 V and then charged to 1.8 V at 50 mA/g. XRD was collected using a Rigaku Smart Lab diffractometer with copper Kα radiation (λ = 1.5406 Å) from 5 to 80° 2-theta. Transmission XAS Ag K-edge data were collected at the 7-BM beamline of the National Synchrotron Light Source II at Brookhaven National Laboratory in Upton, NY. The beam was calibrated to 25,514 eV using an Ag reference foil. The ion chambers were optimized for 10% and 70% absorbance in the incident and transmission ion chambers, respectively. The pristine, discharged, and charged electrodes were prepared between polyimide tape. XAS spec-

Downloaded on 2019-11-06 to IP 130.199.221.173 address. Redistribution subject to ECS terms of use (see ecsdl.org/site/terms_use) unless CC License in place (see abstract).

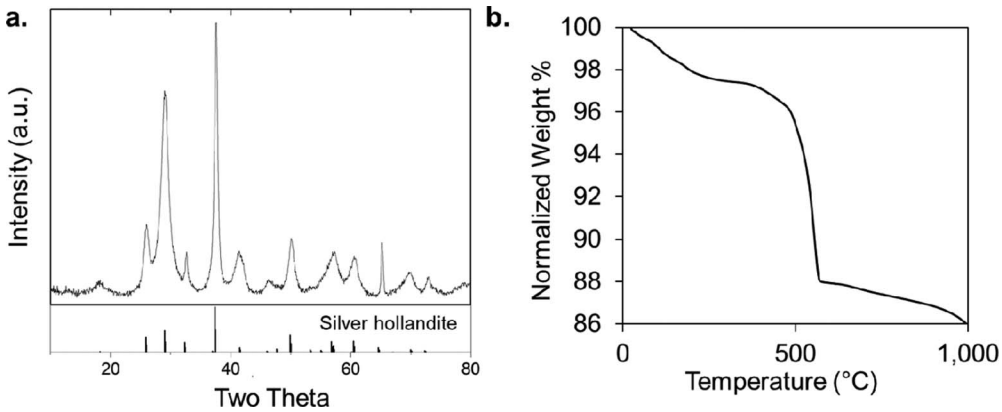

Figure 2. Characterization of silver hollandite, $Ag_{1.5}Mn_8O_{16}$, a. X-ray diffraction and b. thermogravimetric analysis.

tra were calibrated, normalized, and merged using the Athena software package.[31] Each XAS spectrum represents a merge of 16 individual scans.

Results and Discussion

The synthesized sample was characterized through a combination of X-ray diffraction, ICP-OES and thermogravimetric analysis. Analysis of the X-ray diffraction data indicated a phase pure diffraction pattern consistent with silver hollandite.[24] The Scherrer equation was applied to the (211) peak at 37° 2θ, for a crystallite size determination of 15 nm.[32] ICP-OES characterization showed a cationic chemical ratio of 1.46:8 Ag:Mn. TGA analysis was used to quantify the oxygen content of the samples using the method as previously reported.[33–35] Mass loss indicated an oxygen deficiency of 0.04 leading to a final composition of $Ag_{1.46}Mn_8O_{15.96}$. Elsewhere the formula is shown as $Ag_{1.5}Mn_8O_{16}$ for simplicity.

The electrochemistry of the $Ag_{1.5}Mn_8O_{16}$ cathodes was evaluated by cyclic voltammetry in 2M $ZnSO_4$ electrolyte at a scan rate of 0.2mV/s. A sharp peak at around 1.06 V was observed during the 1st cathodic scan (Figure 3a). In the subsequent cycle, the cathodic peak was located at 1.35 V and an overlapped anodic peak at 1.6/1.65 V were apparent. Under galvanostatic cycling, the corresponding voltage profiles were depicted in Figure 3b. In cycle 1 at 50 mA/g, a long plateau at around 1.27 V was observed while in cycle 2, two distinct discharge plateaus at 1.42 V and 1.34 V were present corresponding well with the CV results. The voltage difference between first discharge and second discharge can be ascribed to the potential morphology change of the MnO_2 during electrochemical reactions.[1] The discharge plateaus located at 1.40/1.34 V and the 1.58/1.51 V charge plateaus were previously reported and assigned as either proton conversion (plateau I, 1.40V) or Zn intercalation (plateau II, 1.34V) reactions associated with the crystallographic evolution of MnO_2 during the cycling processes.[1,8]

To probe the reaction mechanism of Ag^+ in Zn/ $Ag_{1.5}Mn_8O_{16}$ batteries, zinc anode cells in 2M $ZnSO_4$ electrolyte were discharged to 1.4, 1.2, 1.0V, and then charged to 1.6V and 1.8V at a current density of 50 mA/g and held at the targeted potentials for 2 hours (Figure 4a). The corresponding electron equivalents per $Ag_{1.5}Mn_8O_{16}$ formula for these electrodes are presented in Table I. EIS data was collected for the pristine material, the sample discharged to 1.4 V, 1.0 V and charged to 1.8 V (Figure 4b). A slight increase in charge transfer resistance was noted during the initial discharge to 1.4V, due to a minimal amount of Ag^0 being displaced at a limited discharge of ~1 mAh/g. Upon subsequent discharge, the interfacial impedance decreased substantially, with the lowest charge transfer impedance evinced at the end of discharge to 1.0V. Upon charge to 1.8V the impedance increases to approach that of the pristine sample. The results of the equivalent circuit fits of the impedance data are shown in Table II.

The impact of reduction on the electrodes was probed where images of recovered cathodes were collected after potential holds to evaluate the changes in morphology, relative size, and local composition as a function of varying potential. SEM images were collected using a

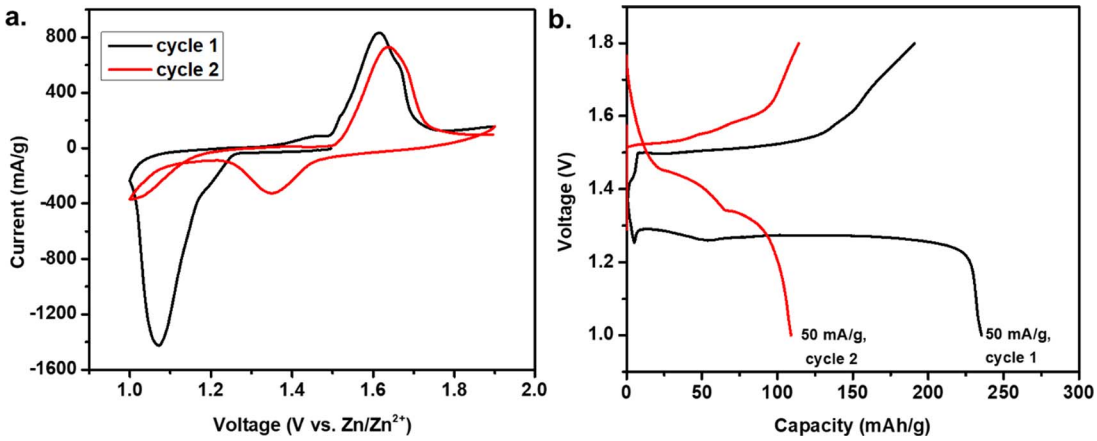

Figure 3. Electrochemistry of $Zn/Ag_{1.5}Mn_8O_{16}$. a. cyclic voltammetry at scan rate of 0.2mV/s, b. discharge/charge curves at 50 mA/g in 2M $ZnSO_4$ electrolyte.

Downloaded on 2019-11-06 to IP 130.199.221.173 address. Redistribution subject to ECS terms of use (see ecsdl.org/site/terms_use) unless CC License in place (see abstract).

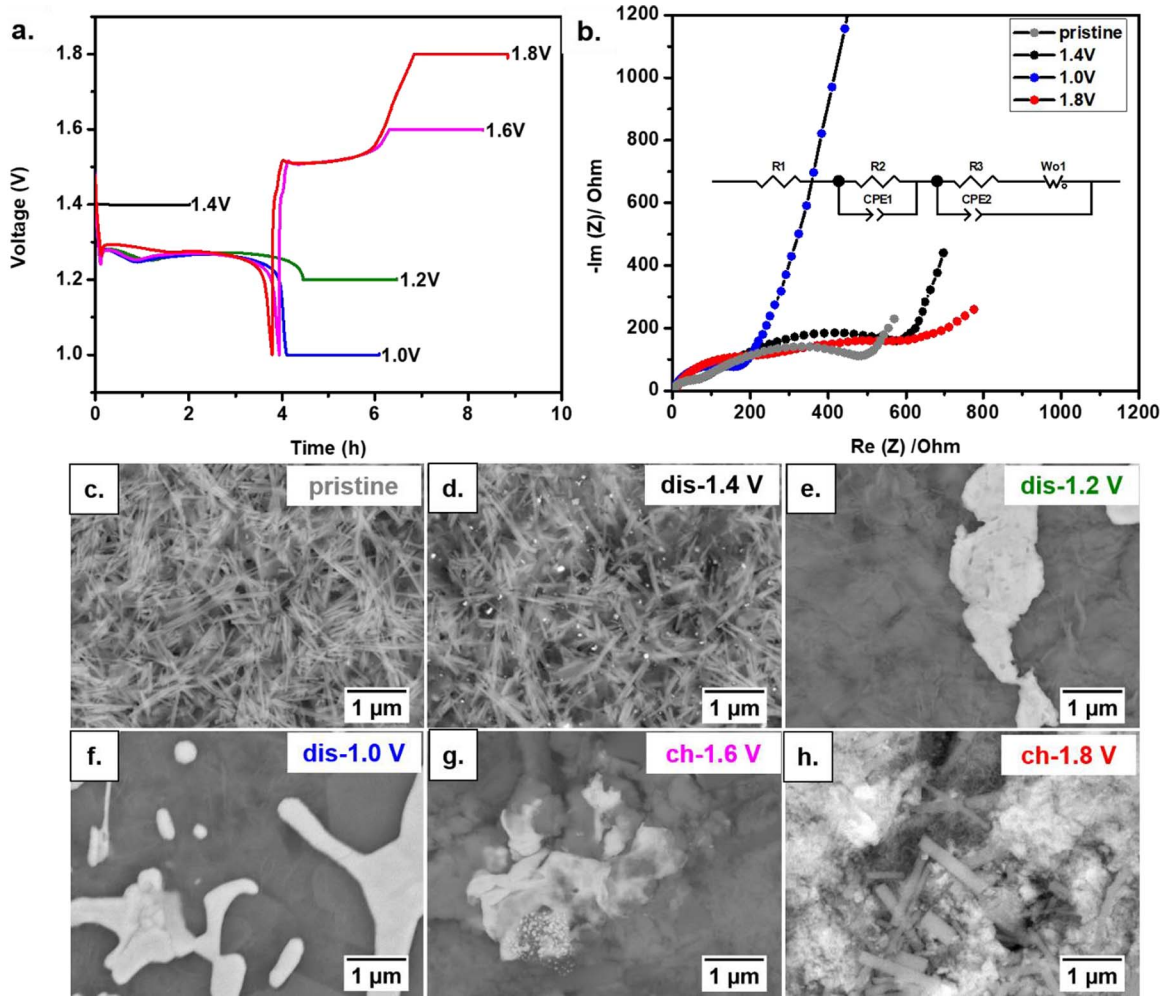

Figure 4. $Zn/Ag_{1.5}Mn_8O_{16}$ cells a. voltage profiles under constant current followed by a constant voltage step for discharge and charge b. EIS results as Nyquist plots, c–h. LABE SEM images of electrodes from a.

low-angle backscattered electron (LABE) detector (Figures 4c–4h) providing signal proportional to the atomic number. The pristine coating electrodes (Figure 4c) evinced an array of nanorods with an average length of $1.3 \pm 0.3\mu m$, average width of $0.08 \pm 0.01\mu m$, and an average aspect ratio of 15. Upon discharge, the LABE SEM images indicated the formation of small and dispersed Ag particles, measuring 39.2 ± 13.0 nm in diameter, starting at 1.4V (Figure 4d). Subsequent discharge to lower voltages of 1.2 and 1.0V led to the formation of large Ag particles with irregular shapes (Figures 4e and 4f, respectively). At 1.0V, there were still nanorods present with a shorter length of $0.5 \pm 0.1\mu m$ in the electrode. Upon charge to 1.6V, the irregular Ag particles were still present (Figure 4g), which disappeared at the end of charge to 1.8V (Figure 4h), consistent with the observed increase in the charge transfer impedance noted in Figure 4b. Ag particles with higher atomic number hence appear to be brighter than those materials with lower atomic numbers.

To further confirm the compositions of the discharge and charge products, EDS maps were collected on the various electrodes prepared at different voltages, displayed in Figure 5, with the corresponding weight percentages of different elements summarized in Table III. No discernible Ag particles were observed in the pristine sample

Table I. Summary of electron equivalents in constant current/ voltage hold test.

Electrode	Electron equivalent constant current	Total electron equivalent: current and potential hold	Electron equivalent during potential hold
Dis to 1.4V	0.03	0.14	0.11
Dis to 1.2V	7.11	7.45	0.34
Dis to 1.0V	6.50	6.88	0.38
Dis/ch to 1.6V	3.79	4.50	0.71
Dis/ch to 1.8V	5.01	6.26	1.25
Dis to 0.8V	7.68	10.87	3.19
Dis to 0.6V	6.38	9.56	3.18

Table II. EIS circuit parameters of the pristine $Zn/Ag_{1.5}Mn_8O_{16}$ cell as well as cells (dis)charged to different potentials at 50 mA/g in 2M $ZnSO_4$ electrolyte.

Cell voltages (V)	R1(Ω)	R2(Ω)	R_{ct}(R3)(Ω)
Pristine (1.49)	2.0	55	461
Discharge to 1.4	2.0	59	505
Discharge to1.0	0.6	-	89
Dis/Charge to1.8V	1.3	80	717

Downloaded on 2019-11-06 to IP 130.199.221.173 address. Redistribution subject to ECS terms of use (see ecsdl.org/site/terms_use) unless CC License in place (see abstract).

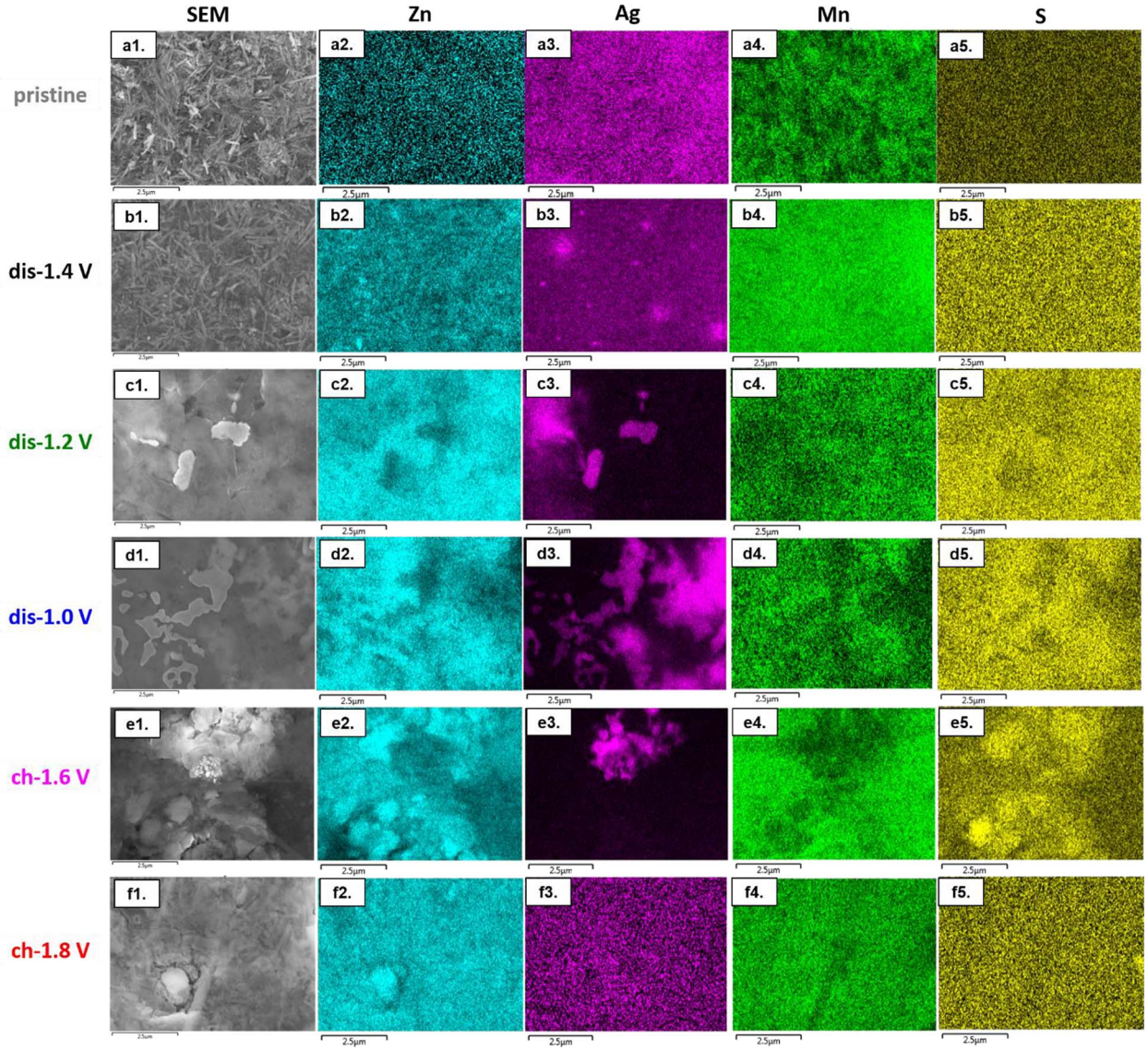

Figure 5. (1) SEM images and (2) EDS elemental maps of $Ag_{1.5}Mn_8O_{16}$ discharged to a. pristine, b. 1.4V, c. 1.2V, d. 1.0V and discharged/charged to e. 1.6V and f. 1.8V (vs. Zn/Zn^{2+}). Scale bar: 2.5 μm.

(Figure 5a), while small Ag nanoparticles were noted in electrodes at 1.4V, which evolved into large irregular particles upon further discharging, and gradually disappeared upon charging to 1.8V. These results agreed well with the aforementioned SEM and EIS data in Figure 4. The EDS determined Ag weight percentages at the electrode surface increased upon discharge and decreased upon charge, as indicated in Table III.

Table III. Weight percentages of elements in (dis)charged electrodes from EDS maps.

Electrodes	O (wt%)	Mn (wt%)	Zn (wt%)	Ag (wt%)	S (wt%)
Pristine	20.1	56.9	0.1	22.8	0.1
D to1.4V	20.3	41.1	20.4	17.1	1.1
D to1.2V	20.9	6.7	54.0	13.3	5.1
D to 1.0V	19.2	5.6	43.3	28.0	3.9
C to 1.6V	24.7	20.7	48.7	1.9	3.9
C to 1.8V	30.7	18.6	48.5	0.6	1.5

The formation of silver metal through a reduction-displacement reaction has been previously observed in the lithiation of silver vanadium phosphorous oxide, specifically $Ag_2VP_2O_8$.[9,36] The Ag^+ in the structure is reduced to Ag^0 as part of the discharge process. In these prior manuscripts detailed analysis of the size of the silver metal formed was reported. Notably, the size of the silver metal formed was dependent both on the composition of the electrode as well as the discharge conditions of the cells. It is likely that the size of the silver metal deposits observed in these experiments are impacted by the experimental conditions.

Scanning vibrating probe (SVP), also referred to as scanning vibrating electrode technique (SVET), was used to comparing a pristine $Ag_{1.5}Mn_8O_{16}$ electrode to electrodes reduced under applied potentials of 0.8V and then 0.6V vs. Zn/Zn^{2+}. A typical SVP output is represented in terms of the potential difference (V_{pp}) across vibration amplitude (peak to peak amplitude, A_{pp}) in relation to the current flux density along the z axis (j_z), and including the solution conductivity, k following Ohm's law, as shown in Eq. 1.[37]

$$V_{pp} = j_z \left(\frac{A_{pp}}{k} \right) \quad [1]$$

Downloaded on 2019-11-06 to IP 130.199.221.173 address. Redistribution subject to ECS terms of use (see ecsdl.org/site/terms_use) unless CC License in place (see abstract).

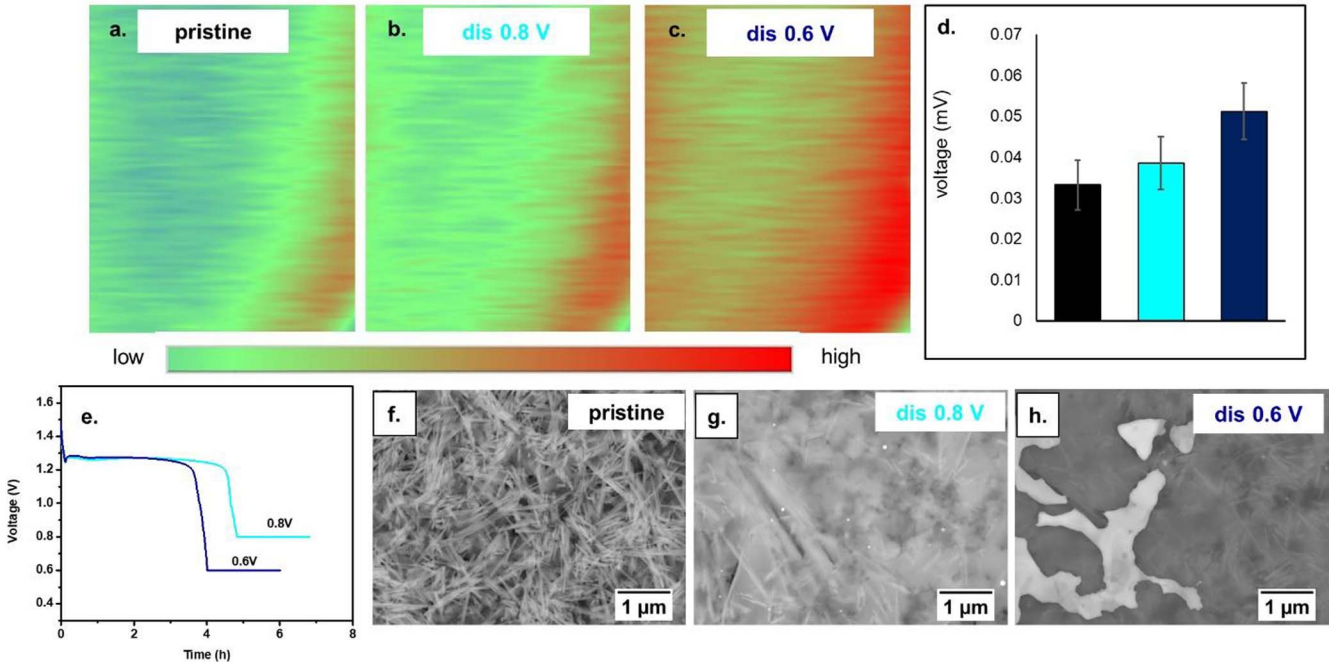

Figure 6. a–c. Scanning vibrating probe (SVP) maps and d. corresponding histogram for $Ag_{1.5}Mn_8O_{16}$ electrodes; a. pristine, discharged to b. 0.8 V and c. 0.6 V (vs Zn/Zn^{2+}), e. Voltage curve from $Zn/Ag_{1.5}Mn_8O_{16}$ electrochemical cell. f–h. LABE SEM images for $Ag_{1.5}Mn_8O_{16}$ electrodes; f. pristine, discharged to g. 0.8 V and h. 0.6 V (vs Zn/Zn^{2+}).

Therefore the current density, j ($\mu A/cm^2$) can be calculated by obtaining the measured electric potential (ΔV), solution conductivity, (k), and vibration amplitude, d (cm) as shown in Eq. 2.[38]

$$j = -\Delta V \frac{k}{d} \quad [2]$$

The above makes the assumption that the electric field around the probe is constant.

Obtained SVP maps of $Ag_{1.5}Mn_8O_{16}$ electrodes are shown in Figures 6a–6c. The sample-probe distance remained the same throughout the successive applied potentials and SVP mapping measurements, with consistent scale used for the images. A lock-in amplifier demodulates the AC signal from the electrometer, so the obtained values represent a DC voltage which is proportional to the vibrating probe signal. Therefore, an increasing DC voltage would imply an increasing current density along the axis of probe vibration, as shown in Eq. 1. For the pristine sample (Figure 6a), there is small variation in signal, mainly near the right most edge over the scanned area suggesting, there is generally good uniformity of the electrode sample. After applying a potential equivalent to 0.8V (vs. Zn/Zn^{2+}), the overall intensity increased (Figure 6b). The signal continued to increase in intensity upon additional electrochemical reduction to the 0.6V applied potential (Figure 6c). The individual SVP data were aggregated to determine average and standard deviation in the DC voltage, and the measurements for the pristine and 0.6V conditions were found be statistically different (Figure 6d). To further probe the change in conductivity, additional electrodes were discharged in coin cells with $ZnSO_4$ electrolyte to the same potentials used in the SVP experiment, using constant current discharge followed by 2 hour potential holds (Figure 6e). The corresponding LABE SEM images (Figures 6f–6h) showed the pristine electrode to be silver free (Figure 6f), with small and dispersed Ag particles present in the sample discharged to 0.8V (Figure 6g), which subsequently transformed to larger Ag particles with irregular shape in the 0.6V sample (Figure 6h).

Scanning vibrating probe (SVP) was used to map a pristine $Ag_{1.5}Mn_8O_{16}$ electrode and then under applied potentials of 0.8 V, 0.6 V, and finally 1.8 V vs. Zn/Zn^{2+}. The obtained SVP maps of the $Ag_{1.5}Mn_8O_{16}$ electrode are shown in Figures 7a–7j. The sample-probe distance remained the same throughout the successive applied potentials and SVP mapping measurements, with consistent scale used for the images. For the pristine sample (Figure 7a), there is little variation in signal suggesting that the electrode was reasonably uniform. After applying a potential of 0.8 V (vs. Zn/Zn^{2+}), the overall intensity increased (Figure 7b). After further reduction at 0.6 V, the intensity decreased somewhat but remained more intense than for the pristine (Figure 7c). The electrode was then oxidized at 1.8 V (equivalent of charge) and a dramatic drop of intensity was observed (Figure 7d). The individual SVP data were aggregated to determine average and standard deviation in the DC voltage (Figure 7e). While the average intensities show an increase in potential upon discharge and a decrease during the following charge; the standard deviations are quite high as there is some level of variation within maps over the large 2000 × 2000 µm area measured. To alleviate this problem, the average and standard deviation of a 500 × 500 µm section was determined for each map (Figures 7f–7j). As can be seen in Figure 7j, the changes in intensity previously noted are significant. The increase in intensity upon reduction (discharge), is consistent with the conductivity increasing due to the formation of silver metal. The decrease upon charge suggests that a more insulating species is being formed at the surface.

To further confirm the formation of metallic Ag particles upon discharge, XRD data were conducted over pristine electrodes and electrodes reduced to 1.0 V (vs. Zn/Zn^{2+}) as well as those reduced to 1.0 V followed by charge to 1.8 V, Figure 8. The XRD of the pristine powder in Figure 8a is representative of reported $Ag_{1.3}Mn_8O_{16}$ patterns. The first four peaks at 25.9°, 29.0°, 32.3° and 37.4° correspond to the (220), (310), (101), and (211) reflections of the silver hollandite structure, respectively. After discharge to 1.0 V (Figure 8b), the dominant reflections are located at 8.3°, 16.4° and 24.6°, which correspond to the (001), (002), and (003) reflections of the osakite salt $ZnSO_4(Zn(OH)_2)_3$ similar to previous reports.[1] Presence of Ag^0 is indicated by peaks at 38.3° and 43.7° corresponding to the (111) and (220) reflections of cubic Ag^0. Upon charge (Figure 8c), the (220) and (310) reflections of silver hollandite are present.There

Downloaded on 2019-11-06 to IP 130.199.221.173 address. Redistribution subject to ECS terms of use (see ecsdl.org/site/terms_use) unless CC License in place (see abstract).

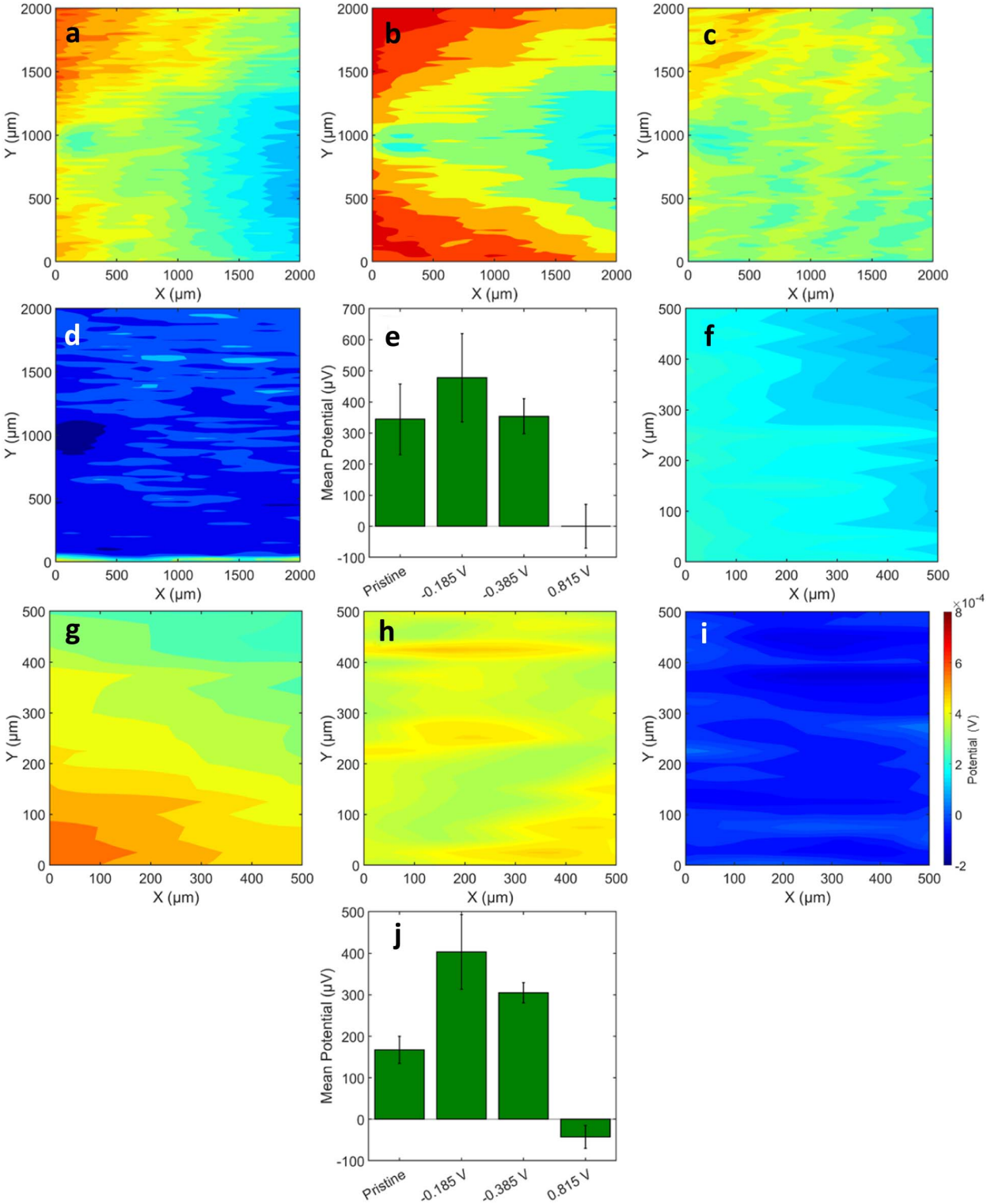

Figure 7. SVP maps of silver hollandite coated on steel. (a) pristine, (b) discharged to 0.8 V, (c) discharged to 0.6 V, and (d) charged to 1.8 V (vs. Zn/Zn^{2+}). (f) section map of (a), (g) section map of (b), (h) section map of (c) and (i) section map of (d) from x = 1500-2000 and y = 75-575. (e) and (j) show the average potential of the full maps and the section maps, respectively. Voltages showing in (e) and (j) are relative to Ag/AgCl.

are no peaks associated with osakite or Ag^0 in the XRD pattern of the charged sample. Thus, ex-situ XRD results suggest that Ag^0 is formed upon discharge to 1.0 V with reversibility to Ag^+ upon charge to 1.8 V.

Further evidence of Ag° formation was gained using X-ray absorption spectroscopy measurements (Figure 9) at the Ag K-edge. Upon discharge to 1.0 V, there is a clear peak in the EXAFS spectrum at ∼2.9 Å, analagous to the major defining feature of the Ag^0 reference foil. Upon charge to 1.8 V, this peak is no longer present, consistent with the XRD results noting the disappearance of the Ag^0 pattern.

Downloaded on 2019-11-06 to IP 130.199.221.173 address. Redistribution subject to ECS terms of use (see ecsdl.org/site/terms_use) unless CC License in place (see abstract).

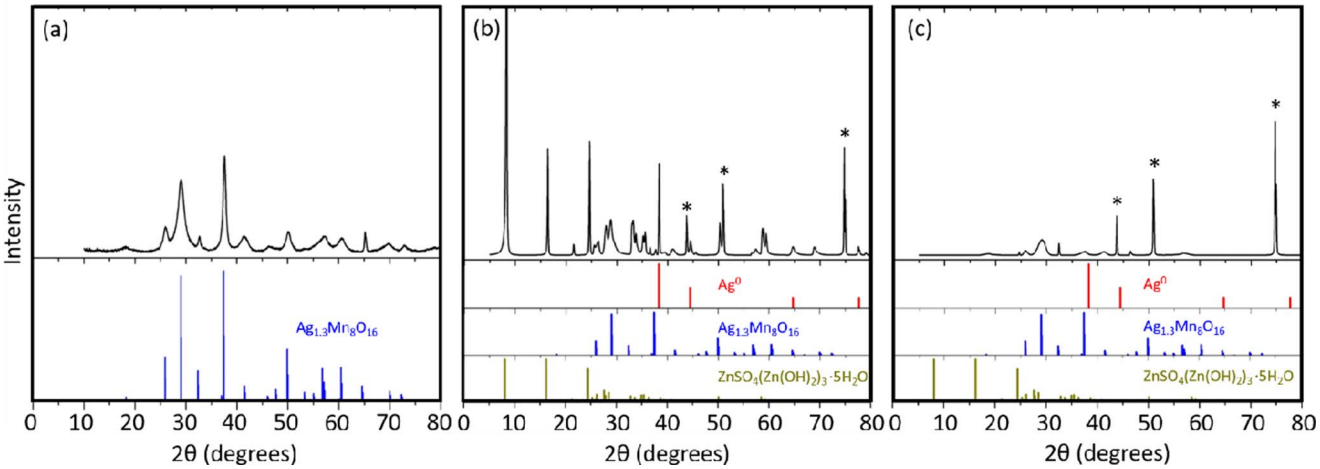

Figure 8. XRD patterns of (a) a pristine 15 nm $Ag_{1.4}Mn_8O_{16}$ powder, (b) an electrode discharged to 1.0 V vs. Zn, and (c) an electrode discharged to 1.0 V then charged to 1.8 V vs. Zn. Asterisks denote peaks attributed to the stainless steel current collector.

The XANES spectra for a pristine silver hollandite electrode and an electrode after discharge to 1.0 V were compared to MnO_2, Mn_2O_3, and MnO powder standards in Figure 10a. The edge position of the pristine electrode is 6551.6 eV and between the edge positions of MnO_2 (6557eV) and Mn_2O_3 (6549eV) standards, suggesting a mixed $Mn^{3+/4+}$ oxidation state. As a result of discharge to 1.0 V, the XANES region is located at a lower energy and is comparable to the Mn_2O_3 standard, suggesting a Mn^{3+} oxidation state. The μ-XRF maps for the pristine electrode (Figure 10b) and reduced electrodes measured after discharge to 1.0 V (Figure 10c) and charge to 1.8 V (Figure 10d) demonstrate that the Mn distribution in the electrodes remains relatively homogenous during the first discharge cycle.

The analysis of the reduced and then oxidized $Ag_{1.5}Mn_8O_{16}$ electrodes collectively showed that submicron sized Ag particles were initially visible on slight discharge to 1.4V versus Zn/Zn^{2+}. On reduction to 1.2V (∼7 electron equivalents per $Ag_{1.5}Mn_8O_{16}$ formula) large islands of silver metal several microns across were evident and remained apparent with further reduction to 0.6V. Subsequent charging of the electrodes to 1.8V resulted in the Ag particles being oxidized to Ag^+ as they are no longer apparent on the surface of the electrodes (Figures 4 and 5). The formation of silver metal is consistent with the previous observation in the non-aqueous Li and Na systems.[6,18] The formation of silver metal early in the discharge is more consistent with reduction by Na ions in non-aqueous media perhaps related to the cation radii of Li^+, Na^+ and Zn^{2+} of 0.4, 1.02 and 0.74Å, respectively. It is worth noting that in the previous studies in non-aqueous media, the Ag^+ to Ag^0 reduction was found to be irreversible with no indication of silver metal oxidation under the test conditions. By contrast, in an aqueous environment, the reduction of Ag^0 occurs early in the discharge process and exhibits subsequent oxidation of the silver metal.

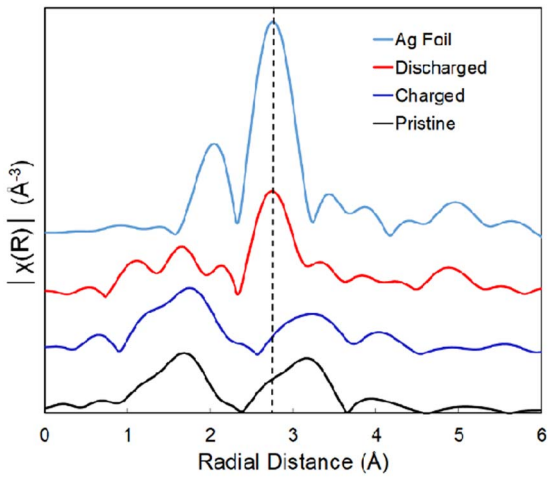

Figure 9. Ag K-edge Fourier transform of EXAFS for pristine, discharged, and charged electrodes compared to Ag metal reference. Fourier transform was conducted using a K range of 2–9 $Å^{-1}$. Data is not phase corrected.

The overall discharge scheme can be represented as shown below. The reduction of Ag(I) to Ag(0) was affirmed by XRD and EXAFS analysis of reduced electrodes. The reduction of Mn(IV) to Mn(III) was noted from the XANES data. Likely due to the nanocrystalline nature of the starting silver hollandite, a crystalline reduced phase of manganese oxide was not apparent.

Cathode:

$$H_2O \rightarrow H^+ + OH^-$$
$$Mn\,(IV) + e^- \rightarrow Mn\,(III)$$
$$Ag\,(I) + e^- \rightarrow Ag\,(0)$$
$$1/2\,Zn^{2+} + OH^- + 1/6\,ZnSO_4 + x6\,H_2O \rightarrow 1/6\,ZnSO_4[Zn(OH)_2]_3 \cdot xH2O$$

Anode:

$$Zn \rightarrow Zn^{2+} + 2e^-$$

Conclusions

Silver hollandite nanorods were prepared using a reflux method yielding $Ag_{1.5}Mn_8O_{16}$ nanorods as characterized by XRD, ICP-OES and TGA. The reduction and subsequent oxidation of the material was explored in aqueous $ZnSO_4$ electrolyte for the first time. A discharge capacity of ∼240 mAh/g was observed for the first reduction of the material. Characterization of the samples at various states of reduction and followed by oxidation were examined by a combination of XRD, SEM, EDS mapping results. Further, the electrochemistry was further studied by using the scanning vibrating probe technique. Ag metal formation upon reduction was confirmed by XRD and EXAFS results accompanied by decrease in charge transfer impedance, as determined by the EIS data. On charge, the appearance of the silver metal disappeared indicating oxidation of the silver centers in the aqueous electrolytes. This stands in interesting contrast to the reduction/oxidation electrochemistry in non-aqueous media where irreversible formation of silver metal was observed.

Downloaded on 2019-11-06 to IP 130.199.221.173 address. Redistribution subject to ECS terms of use (see ecsdl.org/site/terms_use) unless CC License in place (see abstract).

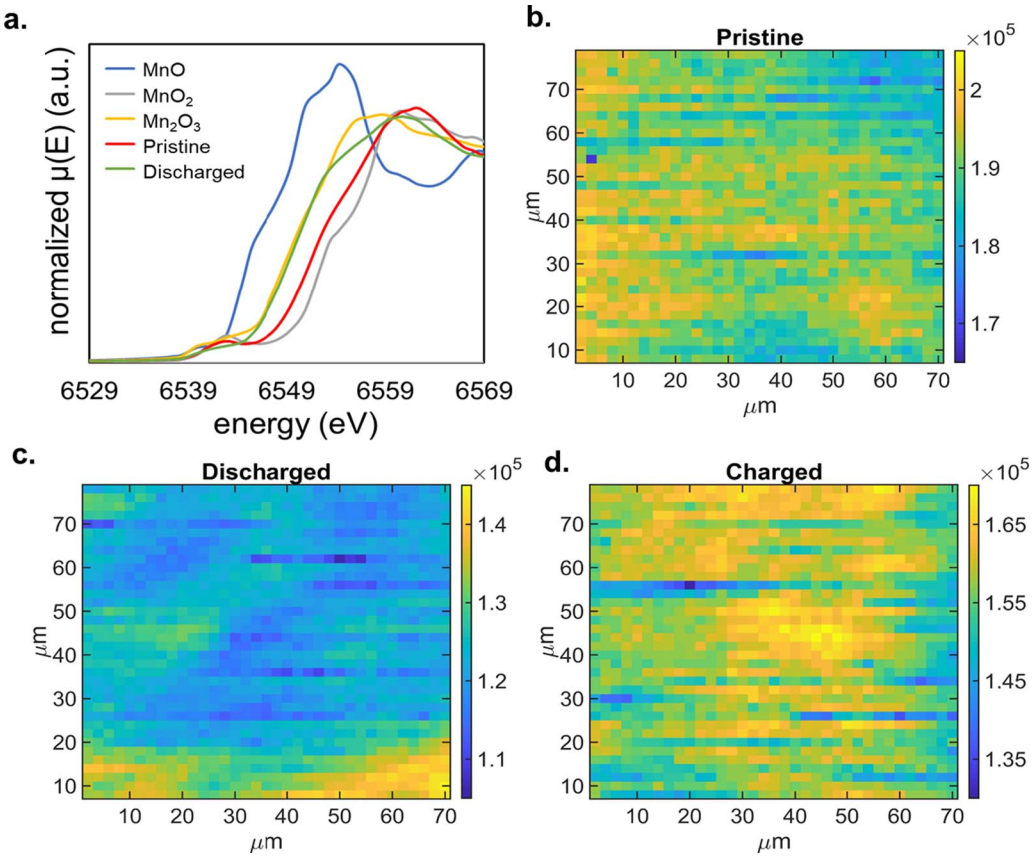

Figure 10. X-ray absorbance spectroscopy data. a. XANES results and b–d. X-ray fluorescence maps for $Ag_{1.5}Mn_8O_{16}$ electrodes: b. pristine, c. discharged to 1.0V and discharged-charged to 1.8V (vs. Zn/Zn^{2+}).

Acknowledgment

Material synthesis and characterization of the pristine samples was supported as part of the Center for Mesoscale Transport Properties, an Energy Frontier Research Center supported by the U.S. Department of Energy, Office of Science, Basic Energy Sciences, under award #DE-SC0012673. The aqueous electrochemistry studies were supported by the Department of Energy, Office of Electricity, administered through Sandia National Laboratories, Purchase Order #1955692. ACM acknowledges Brookhaven National Laboratory for support of the SVP research. Experimental characterizations were carried out in part at the Center for Functional Nanomaterials, Brookhaven National Laboratory, an Office of Science User Facility, which is supported by the U.S. Department of Energy, Office of Basic Energy Sciences, under Contract No. DE-SC0012704. This research used beamlines 5-ID (SRX) and 7-BM (QAS) of the National Synchrotron Light Source II, a U.S. Department of Energy (DOE) Office of Science User Facility operated for the DOE Office of Science by Brookhaven National Laboratory under Contract No. DE-SC0012704. The authors express their sincere gratitude to beam line scientists Steven Ehrlich (QAS), Juergen Thieme (SRX) and Andrew Kiss (SRX) for their assistance. EST acknowledges support from the William and Jane Knapp Chair for Energy and the Environment.

ORCID

Lei Wang https://orcid.org/0000-0002-6348-8344
Alyson Abraham https://orcid.org/0000-0002-6087-9219
Patrick J. West https://orcid.org/0000-0002-8717-9538
Esther S. Takeuchi https://orcid.org/0000-0001-8518-1047
Amy C. Marschilok https://orcid.org/0000-0001-9174-0474
Kenneth J. Takeuchi https://orcid.org/0000-0001-8129-444X

References

1. H. Pan, Y. Shao, P. Yan, Y. Cheng, K. S. Han, Z. Nie, C. Wang, J. Yang, X. Li, P. Bhattacharya, K. T. Mueller, and J. Liu, *Nature Energy*, **1**, 16039 (2016).
2. C. Xu, B. Li, H. Du, and F. Kang, *Angewandte Chemie International Edition*, **51**, 933 (2012).
3. J. S. Ko, M. B. Sassin, J. F. Parker, D. R. Rolison, and Jeffrey W. Long, *Sustainable Energy & Fuels*, **2**, 626 (2018).
4. G. Fang, C. Zhu, M. Chen, J. Zhou, B. Tang, X. Cao, X. Zheng, A. Pan, and S. Liang, *Advanced Functional Materials*, **29**, 1808375 (2019).
5. G. Fang, J. Zhou, A. Pan, and S. Liang, *ACS Energy Letters*, **3**, 2480 (2018).
6. J. Huang, A. S. Poyraz, S.-Y. Lee, L. Wu, Y. Zhu, A. C. Marschilok, K. J. Takeuchi, and E. S. Takeuchi, *ACS Applied Materials & Interfaces*, **9**, 4333 (2017).
7. W. Sun, F. Wang, S. Hou, C. Yang, X. Fan, Z. Ma, T. Gao, F. Han, R. Hu, M. Zhu, and C. Wang, *Journal of the American Chemical Society*, **139**, 9775 (2017).
8. Y. Li, S. Wang, J. R. Salvador, J. Wu, B. Liu, W. Yang, J. Yang, W. Zhang, J. Liu, and J. Yang, *Chemistry of Materials*, **31**, 2036 (2019).
9. K. Kirshenbaum, D. C. Bock, C.-Y. Lee, Z. Zhong, K. J. Takeuchi, A. C. Marschilok, and E. S. Takeuchi, *Science (Washington, DC, U. S.)*, **347**, 149 (2015).
10. M. H. Alfaruqi, J. Gim, S. Kim, J. Song, D. T. Pham, J. Jo, Z. Xiu, V. Mathew, and J. Kim, *Electrochemistry Communications*, **60**, 121 (2015).
11. N. Zhang, F. Cheng, J. Liu, L. Wang, X. Long, X. Liu, F. Li, and J. Chen, *Nature Communications*, **8**, 405 (2017).
12. L. M. Housel, L. Wang, A. Abraham, J. Huang, G. D. Renderos, C. D. Quilty, A. B. Brady, A. C. Marschilok, K. J. Takeuchi, and E. S. Takeuchi, *Accounts of Chemical Research*, **51**, 575 (2018).
13. B. Lee, C. S. Yoon, H. R. Lee, K. Y. Chung, B. W. Cho, and S. H. Oh, *Scientific Reports*, **4**, 6066 (2014).
14. M. H. Alfaruqi, J. Gim, S. Kim, J. Song, J. Jo, S. Kim, V. Mathew, and J. Kim, *Journal of Power Sources*, **288**, 320 (2015).
15. K. J. Takeuchi, S. Z. Yau, A. Subramanian, A. C. Marschilok, and E. S. Takeuchi, **160**, A3090 (2013).
16. A. B. Brady, J. Huang, J. L. Durham, P. F. Smith, J. Bai, E. S. Takeuchi, A. C. Marschilok, and K. J. Takeuchi, *MRS Advances*, **3**, 547 (2018).
17. E. S. Takeuchi, A. C. Marschilok, K. Tanzil, E. S. Kozarsky, S. Zhu, and K. J. Takeuchi, *Chemistry of Materials*, **21**, 4934 (2009).

Downloaded on 2019-11-06 to IP 130.199.221.173 address. Redistribution subject to ECS terms of use (see ecsdl.org/site/terms_use) unless CC License in place (see abstract).

18. F. Xu, L. Wu, Q. Meng, M. Kaltak, J. Huang, J. L. Durham, M. Fernandez-Serra, L. Sun, A. C. Marschilok, E. S. Takeuchi, K. J. Takeuchi, M. S. Hybertsen, and Y. Zhu, *Nature Communications*, **8**, 15400 (2017).
19. L. Shan, Y. Yang, W. Zhang, H. Chen, G. Fang, J. Zhou, and S. Liang, *Energy Storage Materials*, **18**, 10 (2019).
20. L. Shan, J. Zhou, M. Han, G. Fang, X. Cao, X. Wu, and S. Liang, *Journal of Materials Chemistry A*, **7**, 7355 (2019).
21. F. Liu, Z. Chen, G. Fang, Z. Wang, Y. Cai, B. Tang, J. Zhou, and S. Liang, *Nano-Micro Letters*, **11** (2019).
22. G. Fang, C. Zhu, M. Chen, J. Zhou, B. Tang, X. Cao, X. Zheng, A. Pan, and S. Liang, *Advanced Functional Materials*, **29**, (2019).
23. K. J. Takeuchi, S. Z. Yau, M. C. Menard, A. C. Marschilok, and E. S. Takeuchi, *ACS Applied Materials & Interfaces*, **4**, 5547 (2012).
24. F. M. Chang and M. Jansen, *Angewandte Chemie International Edition*, **23**, 906 (1984).
25. A. Simões, D. Battocchi, D. Tallman, and G. Bierwagen, *Progress in Organic Coatings*, **63**, 260 (2008).
26. G. Williams and H. N. McMurray, *Journal of the electrochemical Society*, **155**, C340 (2008).
27. K. B. Deshpande, *Corrosion Science*, **62**, 184 (2012).
28. L. F. Jaffe and R. Nuccitelli, *Cell Bio*., 614 (1974).
29. J. Huang, L. M. Housel, L. Wang, A. M. Bruck, C. D. Quilty, A. Abraham, D. M. Lutz, C. R. Tang, A. Kiss, J. Thieme, K. J. Takeuchi, E. S. Takeuchi, and A. C. Marschilok, *Sustainable Energy & Fuels* (2019).
30. A. S. Poyraz, J. Huang, S. Cheng, D. C. Bock, L. Wu, Y. Zhu, A. C. Marschilok, K. J. Takeuchi, and E. S. Takeuchi, *Green Chemistry*, **18**, 3414 (2016).
31. B. Ravel and M. Newville, *Journal of Synchrotron Radiation*, **12**, 537 (2005).
32. J. Huang, L. M. Housel, C. D. Quilty, A. B. Brady, P. F. Smith, A. Abraham, M. R. Dunkin, D. M. Lutz, B. Zhang, E. S. Takeuchi, A. C. Marschilok, and K. J. Takeuchi, *Journal of The Electrochemical Society*, **165**, A2849 (2018).
33. J. Chen, X. Tang, J. Liu, E. Zhan, J. Li, X. Huang, and W. Shen, *Chemistry of Materials*, **19**, 4292 (2007).
34. Y. Tanaka, M. Tsuji, and Y. Tamaura, *Physical Chemistry Chemical Physics*, **2**, 1473 (2000).
35. H. Huang, Y. Meng, A. Labonte, A. Dobley, and S. L. Suib, *The Journal of Physical Chemistry C*, **117**, 25352 (2013).
36. K. C. Kirshenbaum, D. C. Bock, Z. Zhong, A. C. Marschilok, K. J. Takeuchi, and E. S. Takeuchi, *Journal of Materials Chemistry A*, **3**, 18027 (2015).
37. G. Williams, A. J. Coleman, and H. N. McMurray, *Electrochimica Acta*, **55**, 5947 (2010).
38. L. B. Coelho, M. Mouanga, M. E. Druart, I. Recloux, D. Cossement, and M. G. Olivier, *Corrosion Science*, **110**, 143 (2016).

Downloaded on 2019-11-06 to IP **130.199.221.173** address. Redistribution subject to ECS terms of use (see **ecsdl.org/site/terms_use**) unless CC License in place (see abstract).